DE GRUYTER Appl. Rheol. 2020; 30:1–13

Research Article

Rehab N. Al-kaby, Sarah L. Codd, Joseph D. Seymour, and Jennifer R. Brown*

Characterization of velocity fluctuations and the transition from transient to steady state shear banding with and without pre-shear in a wormlike micelle solution under shear startup by Rheo-NMR

https://doi.org/10.1515/arh-2020-0001
Received Sep 16, 2019; accepted Jan 23, 2020

Abstract: Rheo-NMR velocimetry was used to study shear banding of a 6 wt.% cetylpyridinium chloride (CPCl) wormlike micelle solution under shear startup conditions with and without pre-shear. 1D velocity profiles across the fluid gap of a concentric cylinder Couette shear cell were measured every 1 s following shear startup for four different applied shear rates within the stress plateau. Fitting of the velocity profiles allowed calculation of the shear banding characteristics (shear rates in the high and low shear band, the interface position and apparent slip at the inner rotating wall) as the flow transitioned from transient to steady state regimes. Characteristic timescales to reach steady state were obtained and found to be similar for all shear banding characteristics. Timescales decreased with increasing applied shear rate. Large temporal fluctuations with time were also observed and Fourier transform of the time and velocity autocorrelation functions quantified the fluctuation frequencies. Frequencies corresponded to the elastically driven hydrodynamic instabilities, *i.e.* vortices, that are known to occur in the unstable high shear band and were dependent upon both applied shear rate and the pre-shear protocol.

Keywords: Rheo-NMR; magnetic resonance; shear banding

1 Introduction

Newtonian fluids show linear responses under deformation as their structure is not affected by flow. In contrast, complex fluids can often display nonlinear, heterogenous or anisotropic properties when subject to applied stress due to the coupling between the microstructure of a fluid and its flow [1], usually associated with microstructural reorganization of the system. One of the most interesting examples of such a non-linear response is the phenomenon of shear banding which has been reported in complex fluids such as polymer solutions, foams, emulsions, colloidal glasses and wormlike micelles [2–5]. The simple picture of shear banding is the formation of flow into two macroscopic bands with different local shear rates [6].

Among complex fluids that exhibit shear banding, wormlike micelles have attracted considerable theoretical and experimental attention due to their wide use in different applications; including as household and personal care products, viscosity modifiers, electrospun tissue scaffolds, and in oil extraction applications [7–10]. Wormlike micelles are elongated and flexible cylindrical, or rod-like, aggregates typically formed by self-assembly of amphiphilic molecules in an aqueous medium [11]. These fluids possess unique viscoelastic properties due to their entangled network, similar to flexible polymer solutions, but with an ability to break and reform continuously under flow. Hence, they are sometimes called “living polymers” [12]. In the fast breaking limit, these systems behave as monodisperse polymers and obey a Maxwellian viscoelastic model with a single relaxation time λ_R at small deformations [2].

The rheological signature of shear banding in wormlike micelle systems is the presence of a stress plateau in the steady state flow curve that occurs between two critical shear rates. This phenomena was first pointed out experimentally by Rehage and Hoffmann [13]. They showed that the flow is homogeneous below the first critical shear rate

---

***Corresponding Author: Jennifer R. Brown:** Department of Chemical and Biological Engineering, Montana State University, Bozeman MT 59717, United States of America;
Email: jennifer.brown@montana.edu
Rehab N. Al-kaby, Sarah L. Codd: Department of Mechanical and Industrial Engineering, Montana State University, Bozeman MT 59717, United States of America
Joseph D. Seymour: Department of Chemical and Biological Engineering, Montana State University, Bozeman MT 59717, United States of America

$\dot{\gamma}_l$ and beyond the second critical shear rate $\dot{\gamma}_h$. In these regions the shear stress increases monotonically with increasing shear rate. On the other hand, between the two critical shear rates in the stress plateau the flow becomes heterogeneous and the shear rate varies spatially, forming shear bands. In this shear banding region, stress stays nearly constant or varies slightly depending on the curvature of the flow geometry [14]. The wormlike micelles are found to be aligned with respect to the direction of the flow in the high shear band; however, in the low shear band they are entangled and randomly oriented [15, 16]. When wall slip is negligible, the shear banded flow is usually assumed to follow a simple lever rule, in analogy with first-order equilibrium phase transitions, $\dot{\gamma} = \alpha\dot{\gamma}_h + (1 - \alpha)\dot{\gamma}_l$, where $\dot{\gamma}$, $\dot{\gamma}_h$ and $\dot{\gamma}_l$ refer, respectively, to the applied, high and low shear rates and α is the interface position between the high and low shear rate bands. The high and low shear rates, $\dot{\gamma}_h$ and $\dot{\gamma}_l$, correspond to the start and end of the stress plateau in the flow curve. In systems obeying standard lever rule behavior, α increases linearly with an increasing applied shear rate [17, 18].

The simple lever rule picture of the shear banding phenomenon is not always observed [19, 20], instead, unexpected and complex fluctuation dynamics are often seen [19, 21, 22]. Early 1D velocimetry studies connected flow fluctuations to the interplay between wall slip and shear-banding [18, 23, 24]. 2D flow visualizations of shear banded flow explained fluctuations in the main flow by the occurrence of interfacial instabilities [25, 26] that caused undulations in the interface position along the vorticial direction and, at higher shear rates, the occurrence of turbulent bursts [27]. Perge *et al.* used two-dimensional ultrafast ultrasonic imaging to spatially map both radial and azimuthal velocity components, showing a vorticial flow structure in the high shear rate band and suggesting that previous observations of temporal oscillations were linked to the secondary flow features [28]. It became clear that elastic instabilities were manifesting in the high shear band as pairs of Taylor vortices, which cause undulations along the interface in the vorticial direction. The vortices are due to elastic instability in shear banded WLM solutions [26], unlike the traditional Taylor vortices seen in Couette flow that are of inertial origin [29].

2D studies suggested that the periodic or chaotic fluctuations observed previously in 1D velocity measurements could be attributed to the 3D nature of the flow field. In other words, spatial heterogeneity contributes to the temporal dynamics of the shear banded flow. The work of Fardin and co-workers [26] have made clear that the using of 1D velocimetry alone is not enough to definitively deduce the presence of instabilities in the shear banded flow or quantitatively characterize them.

In a previous study [30], we have used Rheo-NMR velocimetry, a technique that incorporates rheometric shear cells into a nuclear magnetic resonance (NMR) spectrometer, to show that high temporal resolution 1D velocity measurements have the potential to provide valuable information in spite of, and even informing about, the 3D flows. 1D velocity profiles were acquired across the fluid gap of a concentric cylinder shear cell as a function of time following shear startup to a single applied shear rate in order to analyze the evolution of the shear banded flow from transient to steady state regimes and study the impact of pre-shear protocols on the fluid response [30]. The Fourier transform of the time and velocity autocorrelation functions were used to quantify the fluctuation frequencies related to the presence of flow instabilities [30]. In the present paper, we extend this technique and analysis under shear startup conditions for four different applied shear rates within the stress plateau, in order to further connect temporal fluctuations in 1D measurements to 3D hydrodynamic instabilities. We extract quantitative timescales of the shear banded flow to evolve from transient to steady state regimes and analyze the impact of pre-shear protocols and shear rate on the shear banding characteristics and fluctuation frequencies following shear startup.

2 Materials and methods

2.1 Sample preparation

A 6 wt.% cetylpyridinium chloride (CPCl) and sodium salicylate (NaSal) solution with a molar ratio [NaSal]/[CPCl] = 0.5 in 0.5 M NaCl-brine was used in this work. In order to acquire NMR velocity profiles more quickly, 0.2% $GdCl_3$ was added to reduce the ^1H NMR relaxation time. From rheological measurements, the addition of 0.2% $GdCl_3$ did not change the mechanical behavior of the sample. All the materials were purchased from Sigma-Aldrich. To prepare the samples, all components were mixed for 120 min at a temperature of 45°C and then stored at 30°C for at least one month before experiments were conducted. To prevent degradation of the samples, they were stored in a container preventing ambient light exposure conditions. This system has been extensively studied and is well-known to form elongated wormlike micelles [31].

2.2 Rheometry

The linear and nonlinear rheological measurements were performed at 25°C under controlled strain using a TA instruments AR-G2 rheometer equipped with a steel cone-and-plate geometry with a 60 mm diameter and a 2° angle. The linear viscoelastic measurement (data not shown) exhibits a single mode Maxwellian behavior with characteristic relaxation time λ_R = 0.436 s and plateau modulus G_o = 100 Pa, consistent with the literature [26]. The steady flow curve (Figure 1) shows a stress plateau from $\dot{\gamma}_l \approx$ 2.6 s^{-1} to $\dot{\gamma}_h \approx$ 24 s^{-1}. The values of $\dot{\gamma}_l$ and $\dot{\gamma}_h$ were found following the procedure of Salmon *et al.* [24] and agree with values reported in the literature [26]. In the flow curves, the torque at each applied shear rate had reached steady state to within 5% tolerance for 3 consecutive data points (collected every 10 s) by the time of data collection.

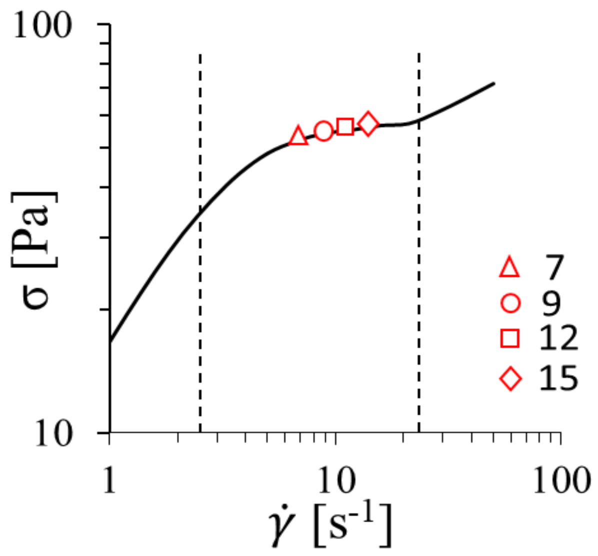

Figure 1: Stress vs applied shear rate for 6% CPCl/NaSal wormlike micelle solution, exhibiting a stress plateau characteristic of shear banding that extends from $\dot{\gamma}_l \approx$ 2.6 s^{-1} to $\dot{\gamma}_h \approx$ 24 s^{-1} (region between the two dashed lines). The red symbols correspond to the four different applied shear rates [s^{-1}] used in shear startup experiments, demonstrating where these shear rates fall in the stress plateau.

2.3 Rheo-NMR

A Rheo-NMR Couette cell with a glass stator and a polyether ether ketone (PEEK) rotor with a roughened cross hatched surface was used for all Rheo-NMR experiments. The outer and inner radii of the shear cell were R_o = 9 and R_i = 8 mm, respectively, resulting in a fluid gap of 1 mm and a radius ratio ($\kappa = R_i / R_o$) of 0.89. All Rheo-NMR measurements were carried out at T = 22°C, above the Krafft temperature of 21.5°C. To control temperature, a thermo electron corporation (Merline M25) recirculating chiller was used. To monitor temperature, a thermocouple inside the NMR probe at the base of the resonator coil and bottom of the Rheo-NMR shear cell was used.

A Bruker AVANCE 300 spectrometer equipped with a Micro-2.5 gradient system (maximum Gradient: 1.5 T/m 60A) and a 25 mm birdcage resonator coil, along with Bruker Topspin software, was used to acquire Rheo-NMR data. Prospa (Magritek, Wellington NZ) software was used for data analysis. Pulsed gradient spin echo (PGSE) motion encoding [32] with double slice selection and 1D image acquisition, as depicted in Figure 2 [33], was used to acquire 1D velocity images. Rf pulse durations were 52 µs for the 90 degree excitation pulse and 104 µs for the two 180 degree refocusing pulses. The echo time was TE = 55 ms and the repetition delay was TR = 217 ms. 1D velocity profiles across the fluid gap (velocity gradient direction; x-axis) had a spatial resolution of 59 µm (FOV = 30 mm and 512 points). The imaging region (Figure 2b) was a slab with a 10 mm thick slice selected along the vorticity direction (z-axis) and a 1 mm thick slice along the velocity direction (y-axis). Velocity was measured in the direction of flow (y-axis). The displacement observation time was Δ = 11 ms, magnetic field gradient pulse durations were δ = 1 ms and two flow encoding gradient steps were done. For these repetition and acquisition times, two signal averages and two flow encoding gradient steps, the total experiment time for a single velocity measurement was 1 s.

The 1D velocity profiles were acquired every 1 s across the fluid gap of the Rheo-NMR concentric cylinder Couette geometry under shear startup conditions for four different applied shear rates ($\dot{\gamma}$ = 7, 9, 12, and 15 s^{-1}). The applied shear rate for the small fluid gap used in this work can be approximated as constant and equal to $\dot{\gamma} = v_{max}/e$, where v_{max} is the velocity of the rotating inner cylinder and e is the fluid gap [35]. To quantify the characteristics of the shear banded flow, the high and low shear band regions of the 1D velocity profiles were fitted linearly and the slopes of the lines provided the values of the shear rate $\dot{\gamma}_h$ and $\dot{\gamma}_l$ for the high and low shear band respectively. The intersect of the lines gave the interface position α. The velocity profiles are plotted as a function of position x normalized by e with x = 0 defined as the inner rotor wall while x = 1 corresponds to the outer stator wall. To evaluate the apparent wall slip, following Fardin and LeRouge [36], a "true" shear rate $\dot{\gamma}_{true}$ was calculated as $\dot{\gamma}_{true} = |v(0) - v(e)|/e$.

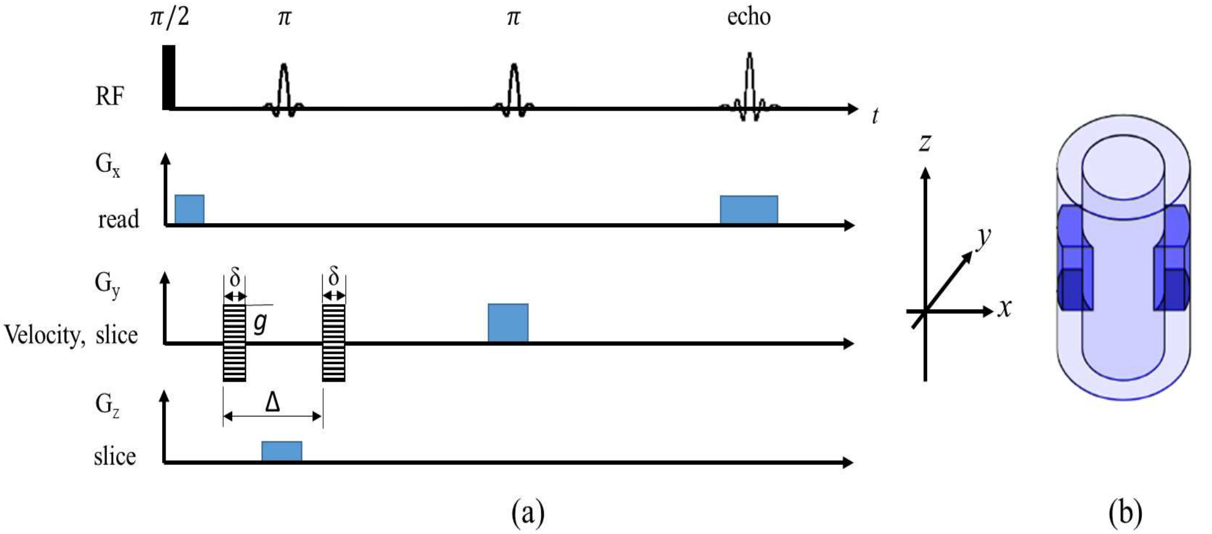

Figure 2: (a) Timing diagram for PGSE motion encoding with double slice selection. (b) A schematic of the Couette. The imaging region, consisting of a 10 mm thick slice along the vorticity direction (*z*-axis) and a 1 mm thick slice along the velocity direction (*y*-axis), is shown in the shaded section. The 1D image had a spatial resolution of 59 µm/pixel and was acquired across the fluid gap (*x*-axis). Velocity was measured in the direction of flow (*y*-axis) with $\Delta = 11$ ms and $\delta = 1$ ms. The inner cylinder, the rotor, is rotating and the outer cylinder, the stator, is stationary.

2.4 Experimental protocols

Two different experimental protocols were used in this work:

- Protocol 1 (no pre-shear): between each shear startup experiment, the system was allowed to return to an isotropic equilibrium state by resting the sample for a wait time $t_w = 300$ min.
- Protocol 2 (with pre-shear): prior to each shear startup experiment, a fixed pre-shear of 10 s^{-1} was applied for 1 min, followed by 2 min of rest. This protocol has been used previously in the literature in an attempt to ensure homogenization [34].

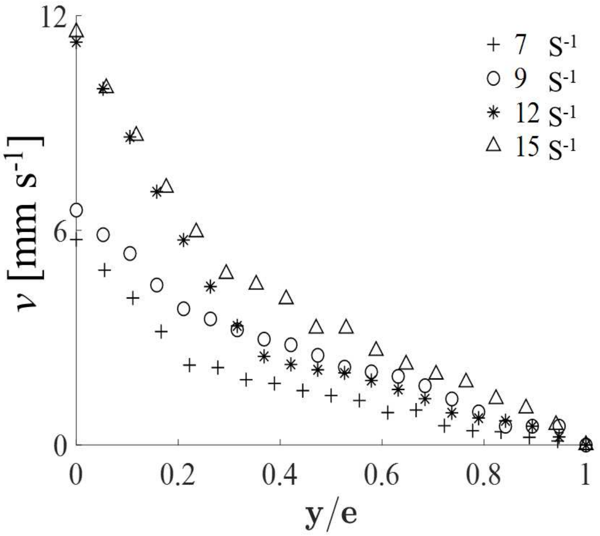

Figure 3: 1D velocity profiles across the normalized fluid gap y/e at steady state for different shear rates, showing shear banding, where e refers to the fluid gap width of 1 mm.

3 Results

Representative velocity profiles at steady state for all applied shear rates are shown in Figure 3, showing shear banding. Linear fitting of each 1 s velocity profile was performed as described in the methods and in previous work for 12 s^{-1} [30] and the resulting shear banding characteristics (α, $\dot{\gamma}_h$, $\dot{\gamma}_l$, and $\dot{\gamma}_{true}$) are shown in Figure 4 as a function of time following startup for an applied shear rate of 15 s^{-1} using shear startup protocols without pre-shear (protocol 1) and with pre-shear (protocol 2).

As shown in previous work [30], the velocity and therefore shear banding characteristics exhibit large temporal fluctuations following an abrupt startup. As indicated in the literature and supported by the results of this study presented below, these fluctuations are due at least partially to a fluctuating slip at the inner rotor wall and the presence

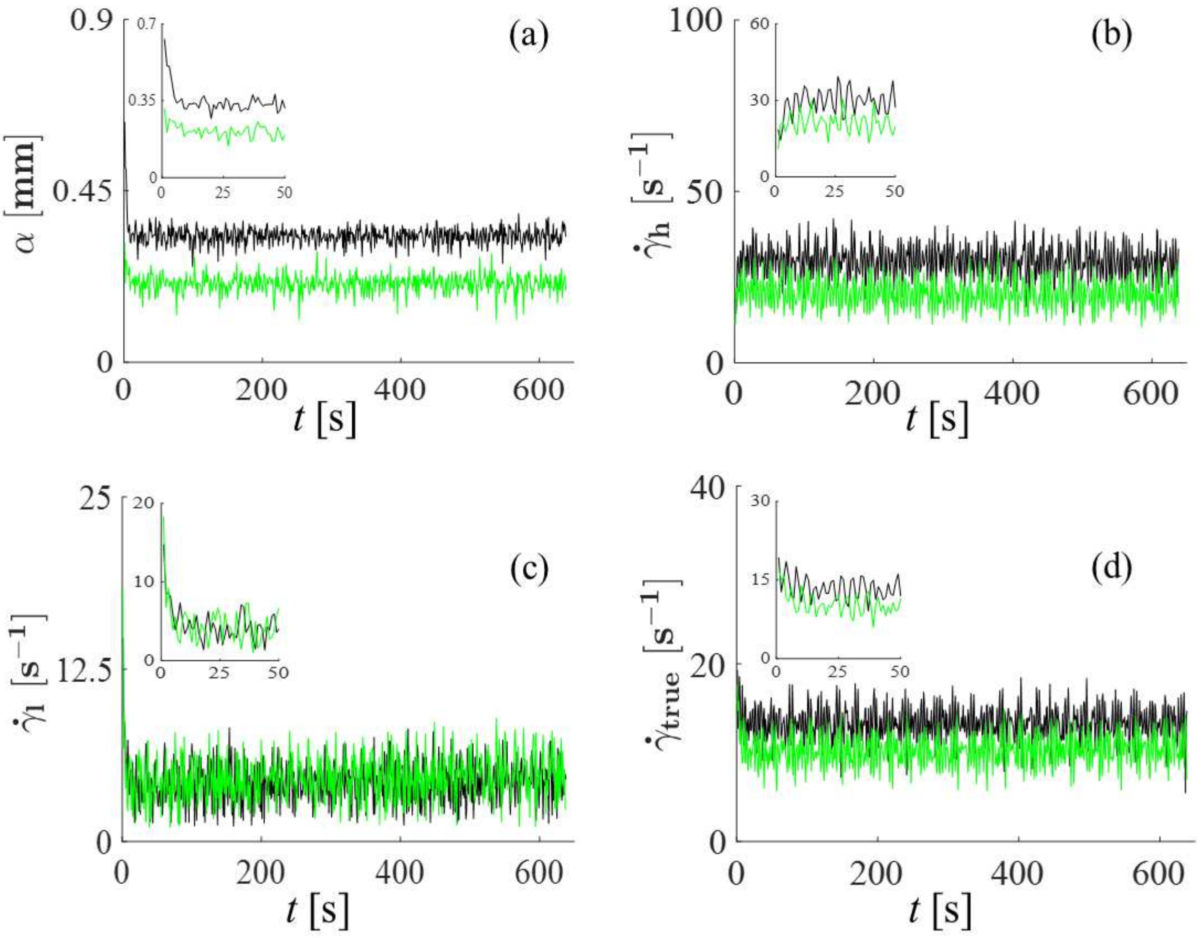

Figure 4: (a) the interface position α, (b) the shear rate in the high shear band $\dot\gamma_h$, (c) the shear rate in the low shear band $\dot\gamma_l$ and (d) the true shear rate $\dot\gamma_{true}$ obtained from 1D velocity profiles acquired every 1 s as a function of time following shear startup to 15 s^{-1}. The black line is protocol 1 (no pre-shear) and the green line is protocol 2 (with pre-shear). The evolution from transient to steady state values is visible in the first 50 seconds (shown in the insets) as well as large fluctuations with time for the entire acquisition duration.

of secondary flow components due to flow instabilities that manifest as fluctuations in a 1D measurement [26, 28].

All the shear banding characteristics follow behavior similar to that reported in the literature [18, 25] and our previous work [30] and was consistent for multiple trials. Immediately following startup, the velocity profile is linear in the initial few seconds prior to shear band formation, corresponding to the large stress overshoot in the bulk mechanical response. This is reflected in Figure 4(b) and (c) insets where $\dot\gamma_h$ and $\dot\gamma_l$ have the same value initially, as would be expected from a linear velocity profile.

As the shear bands form, the interface position between the shear bands α migrates into the fluid gap until it reaches its steady state position (Figure 4a). During this same time period, $\dot\gamma_h$ increases and $\dot\gamma_l$ decreases until reaching a fluctuating behavior in time about an average value.

Figure 4 also shows that at applied shear rate of 15 s^{-1}, there are clear differences between the two protocols. For protocol 1 (no pre-shear), the interface position (Figure 4a) reaches an average value of $\alpha = 0.33$ at steady state, while for protocol 2 (with pre-shear), the steady state average interface position is $\alpha = 0.21$. When pre-shear is present in the sample, the interface position is located nearer the inner rotor wall. The value for the shear rate in the high shear rate band (Figure 4b) for protocol 1 reaches a steady state average of 29 s^{-1}, roughly consistent with where the stress plateau ends in the flow curve (24 s^{-1}; Figure 1). For protocol 2, the average high shear rate is lower at 20 s^{-1}. The differences here are tied to the amount of slip present. From the values of the true shear rate, we can see that in protocol 1, less slip is present. The average true shear rate for protocol 1 is 13.2 s^{-1}, while for protocol 2, it is 10.4 s^{-1}. If there was no slip then a true shear rate equal to the applied shear

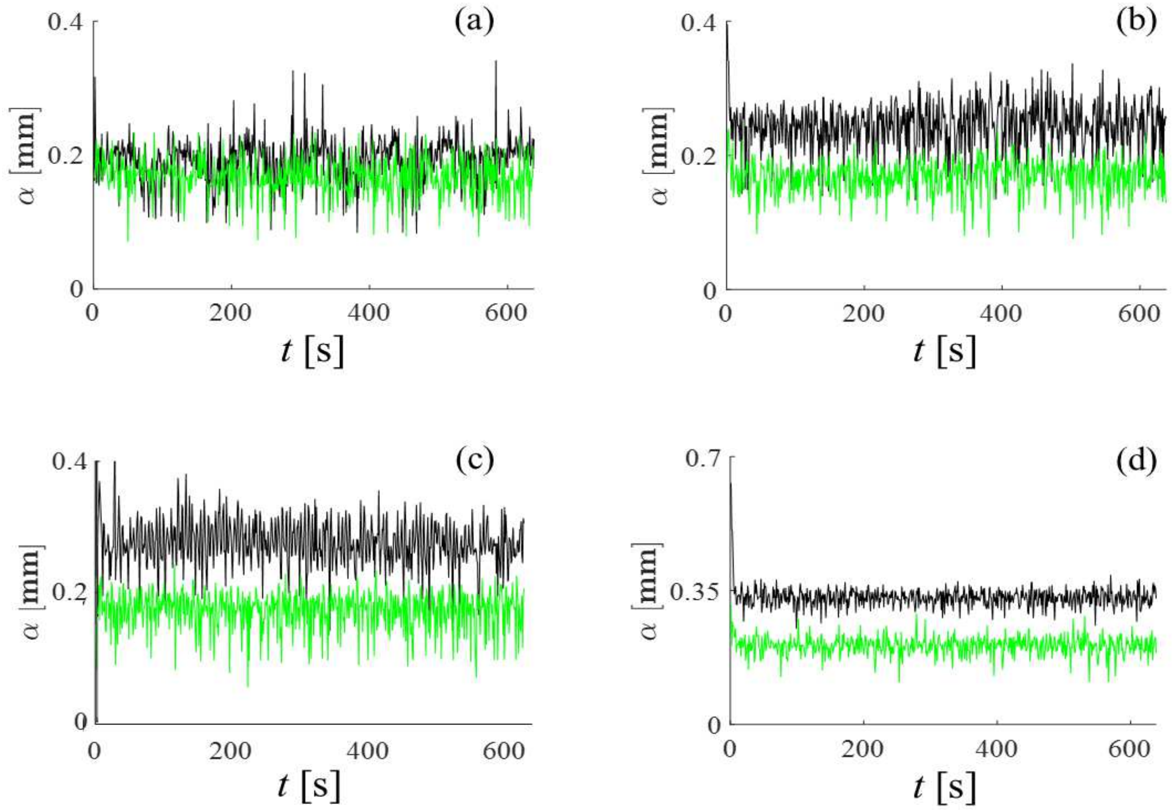

Figure 5: The interface position α obtained from 1D velocity profiles acquired every 1 s as a function of time following shear startup to (a) 7 s^{-1}, (b) 9 s^{-1}, (c) 12 s^{-1} and (d) 15 s^{-1}. The black line is protocol 1 (no pre-shear) and the green line is protocol 2 (with pre-shear).

rate of 15 s^{-1} would be observed. As expected, for protocol 1 with less slip the true shear rate is nearly equal to the applied shear rate and the high shear rate is predicted well by the lever rule and from the flow curve. The differences between protocols are smaller for the low shear band values. The steady state average for protocol 1 is 4.4 s^{-1}, while for protocol 2 it is 4.9 s^{-1}. This is somewhat higher than the $\dot{\gamma}_l = 2.6\ s^{-1}$ that would be expected from the flow curve, as has been seen previously in the literature [25].

Choosing to focus on interface position α (Figure 5), we see that for all four applied shear rates, protocol 1 results in an interface position farther into the fluid gap than for protocol 2. The difference gets larger as the applied shear rate increases.

A Reynolds decomposition approach [37], where variables are decomposed into a time-averaged quantity and a fluctuation about the time average, was used. The velocity profiles were averaged over 25 s and the interface position for these time-averaged profiles was found. The results are plotted in Figure 6. The coarse-grained time averaged values of α are represented by the closed symbols. The solid lines are the average α over the entire experiment. This approach allowed extraction of timescales of the system that were obscured by the fluctuations, so the evolution from the transient to steady state regime could be characterized. In coarse graining approaches, the averaging time must be carefully selected to be longer than the fluctuation timescale τ_f, but shorter than any other timescale that would yield information. The red closed symbols in Figure 6 show the standard deviation of the 25 s time averaged values from the overall mean. The standard deviation captures the variation of the fluctuations from the mean and more clearly reveals the initial transient regime. When the standard deviation plateaus to a constant value, we can assume the system has reached a steady state and the values are minimally fluctuating about the mean. Fluctuations that remain after steady state has been reached are likely to be due to 3D vorticial flow structure in the high shear region. The time it takes for the standard deviation to plateau gives us a timescale for the transition from transient to steady state and the establishment of the 3D vortices. It is not possible to extract this timescale from the data itself due to the fluctuations obscuring the underlying trends.

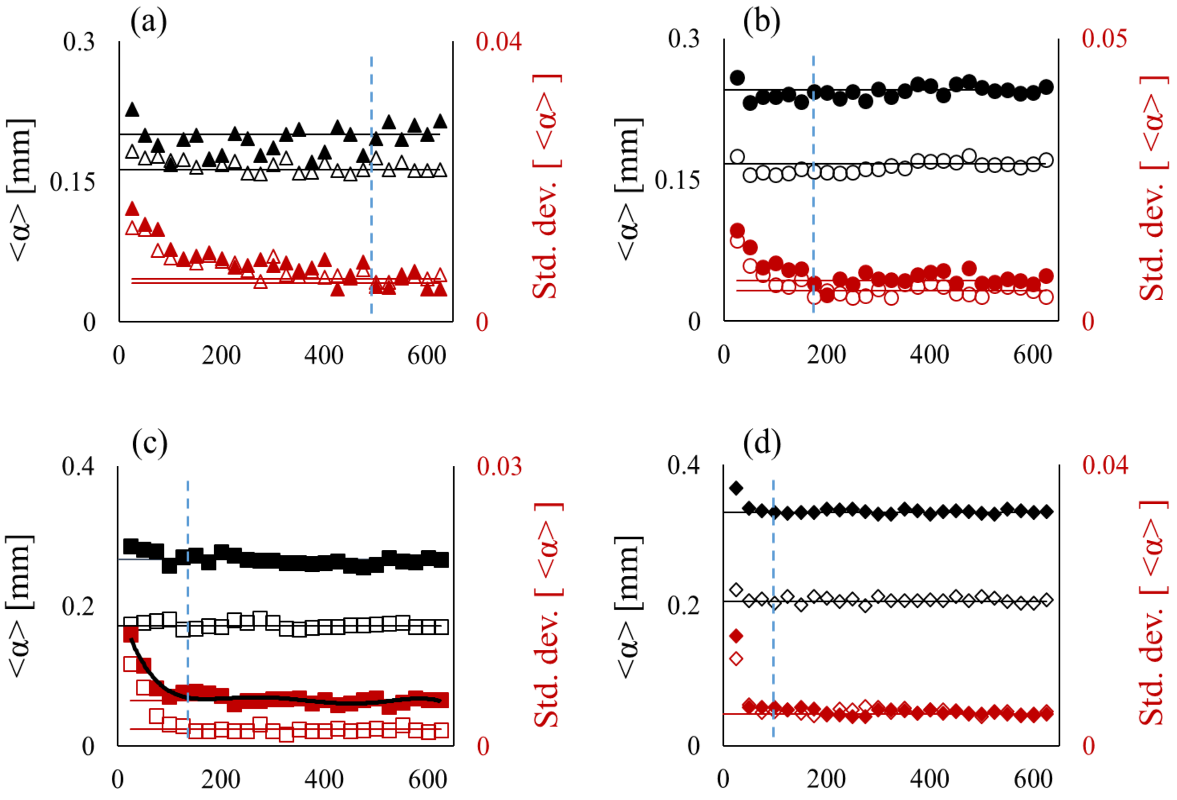

Figure 6: The interface position α averaged over 25 s, a timescale larger than that for the fluctuations, for (a) 7 s^{-1}, (b) 9 s^{-1}, (c) 12 s^{-1} and (d) 15 s^{-1}. Protocol 1 (no pre-shear) is closed black symbols and protocol 2 (with pre-shear) is open black symbols. Solid lines represent the average values for the entire experiment. Red symbols are the standard deviations within each 25 s period (closed symbols are protocol 1 and open symbols are protocol 2). Solid red lines correspond to where the standard deviations plateau. The solid black line over the closed red symbols in (c) demonstrates the data smoothing process used to extract timescales. The dotted blue lines correspond to the steady state timescale τ_{ss}.

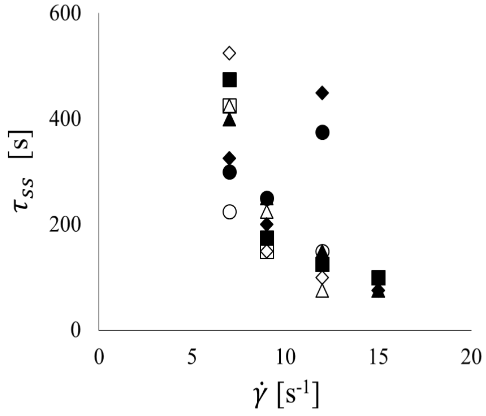

Figure 7: Timescales to reach steady state τ_{ss} as a function of applied shear rate for the interface position (squares), high shear rate (circles), low shear rate (triangles), and true shear rate (diamonds). Protocol 1 (no pre-shear) and protocol 2 (with pre-shear) appear with filled black and open black symbols respectively.

By smoothing the standard deviation data, as shown with the black line over the closed red circles in Figure 6c, we can see where the end of the transient regime occurs *i.e.*, when the standard deviation reaches a plateau as shown by the solid red line. The dashed vertical blue lines show visually when the plateau in the standard deviation is reached for each shear rate and indicate that the timescale to reach steady state decreases as the applied shear rate increases. The exact values for this timescale were extracted using a data smoothing fitting algorithm and are shown more clearly in Figure 7 where timescales for all four of the shear banding characteristics (α, $\dot{\gamma}_h$, $\dot{\gamma}_l$, and $\dot{\gamma}_{true}$) and the two protocols are plotted at each applied shear rate. There is a negative correlation between the timescale to reach steady state and the applied shear rate.

With the exception of 7 s^{-1}, all the shear banding characteristics (α, $\dot{\gamma}_h$, $\dot{\gamma}_l$, and $\dot{\gamma}_{true}$) have roughly the same characteristic time to reach steady state values at a given applied shear rate, consistent with previous results in the lit-

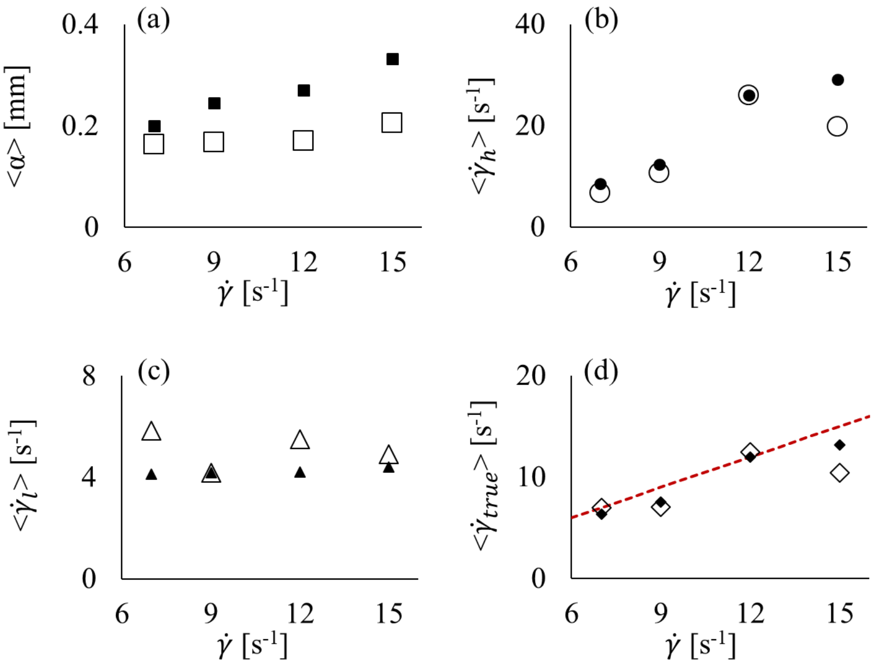

Figure 8: Shear banding characteristics averaged over the last ~120 s of the shear startup experiment, where the flow is at steady state, as a function of applied shear rate for protocol 1 (filled symbols) and protocol 2 (open symbols). Error bars of the standard deviation reflecting the fluctuations in time are smaller than the symbol size. (a) the interface position α (b) the shear rate in the high shear band $\dot{\gamma}_h$, (c) the shear rate in the low shear band $\dot{\gamma}_l$ and (d) the true shear rate $\dot{\gamma}_{true}$, which is a measure of apparent wall slip. The dashed red line is where $\dot{\gamma}_{true} = \dot{\gamma}_{app}$ and values on this line indicate no slip occurring.

erature for 10% CPCl [25]. There is little difference in this timescale between the protocols, indicating that pre-shear does not impact the time it takes for the flow to reach a steady state.

As noted above, the biggest spread in values occurs at 7 s^{-1}. For example, the longest timescale is for the true shear rate for protocol 2 (~525 s) and the shortest timescale is for the high shear rate for protocol 2 (~225 s). This is likely because at an applied shear rate of 7 s^{-1}, we are near the onset of the stress plateau. The high shear band is fairly small (average interface position is 0.20 for protocol 1 and 0.16 for protocol 2) and there is significant variation from the mean, which can be seen in “noisiness” of the time averaged standard deviation. Also, with the longest timescales (~500 s), they are almost on the order of the experiment time (~600 s). Therefore, the timescales obtained using the process of smoothing the data show more disparity.

There are also a few outlier timescales that don’t follow the general decreasing trend with increasing applied shear rate. The true shear rate and high shear rate timescales for applied shear rate 12 s^{-1} are longer (450 and 375 s respectively). In previous work [30] showing the 12 s^{-1} data, we had identified a transient timescale τ_{trans} and a steady state timescale τ_{ss} based on the rate of decrease of the standard deviation. However, evidence of multiple timescales is not seen in the other applied shear rates. As such, we discuss only one timescale τ_{ss} here.

Figure 8 shows the average steady state values of the shear banding characteristics as a function of applied shear rate. For protocol 1, we see behavior as expected from the literature, where the interface position is located further into the fluid gap as the applied shear rate increases farther into the stress plateau (Figure 1). The shear rate in the low shear band (Figure 8c) stays largely constant, behavior also observed in the literature [25]. Following standard lever rule behavior [38], we would expect the shear rates in the low and high shear bands to stay at constant values corresponding to the start and end of the stress plateau respectively ($\dot{\gamma}_l \approx$ 2.6 s^{-1} to $\dot{\gamma}_h \approx$ 24 s^{-1}, as obtained from the flow curve in Figure 1), while the interface position increased linearly. Here, the shear rate in the high shear band increases with increasing applied shear rate. The true shear rate correspondingly also increases with increasing applied shear rate. This behavior has been observed previously [25, 27]. The dashed red line indicates

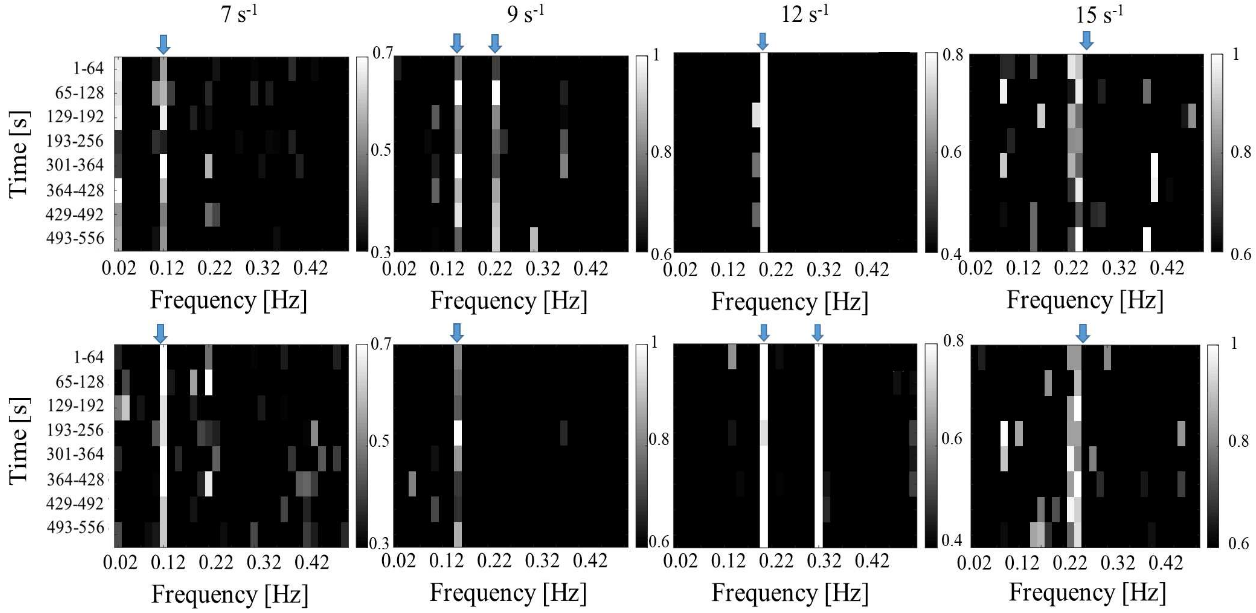

Figure 9: Frequency images from the Fourier transform of the time correlation functions for interface position. The scale bars correspond to amplitude (intensity normalized by the maximum intensity) in arbitrary units (a.u.). The top panels are protocol 1 (no pre-shear) and the bottom panels are protocol 2 (with pre-shear) with increasing shear rate (7, 9, 12 and 15 s^{-1}) from left to right. The dominant frequencies in the spectra are shown with blue arrows.

the case where true shear rate equals applied shear rate and values on this line indicate no slip is present. There is a small amount of slip present only for applied shear rates of 9 and 15 s^{-1} and the amount of slip does not scale with applied shear rate.

For both the high shear rate and the true shear rate, there is little difference between the two protocols. It is only at the highest applied shear rate (15 s^{-1}) that we see any difference. However, both interface position and low shear rate are significantly different for protocol 2 where pre-shear occurs. In protocol 2, we see a much more gradual increase in interface position with increasing applied shear rate and there appears to be a corresponding decrease in the low shear rate that is not seen in protocol 1 (with the exception of applied shear rate 9 s^{-1} which is the same as protocol 1). In general, it appears that pre-shear, which disrupts and homogenizes equilibrium structure, influences the steady state values of low shear rate and location of the interface.

Temporal fluctuations of the four characteristics of shear banding were analyzed by applying a Fourier Transform of the time autocorrelation functions [30] to obtain power spectra. The time domain data were divided into 64 s time intervals following shear startup and time autocorrelation functions were calculated, which were then Fourier transformed to obtain the spectra shown in Figure 9. The fluctuations are not entirely random but reflect the coherent 3D nature of the flow that is due to flow instabilities. Therefore, the fluctuation frequencies may be correlated with the instabilities in the 3D flow. Instabilities manifest primarily as pairs of Taylor vortices in the high shear band, which cause undulations along the interface in the vorticial direction [25, 26, 39]. The vortices are known to travel along the vorticial direction, as opposed to remaining stationary, and their size increases with size of the high shear band as the applied shear rate increases [26]. A 1D measurement cannot fully capture the 3D flow patterns, but full 3D spatially-resolved NMR velocity measurements are too limited in time and spatial resolution to capture the dynamics of the instabilities, such as traveling vortices [40]. Analyzing the fluctuation frequencies as they scale with applied shear rate could be a way to lend insight (or detect) the presence of vortices without the need of a 3D measurement. In Figure 9, as an example we show the spectra for the interface position as a function of flow rate and flow protocol. The blue arrows correspond to the dominant frequencies observed. As can be seen, the amplitude of frequency and also the number of frequencies present depends on both applied shear rate and protocol, but are stable in time. In Figure 10, we have extracted the dominant frequencies for all shear banding characteristics and plotted them against applied shear rate.

In Figures 10(a) and 10(b) we can see there is a frequency that appears in both $\dot{\gamma}_h$ and α for both proto-

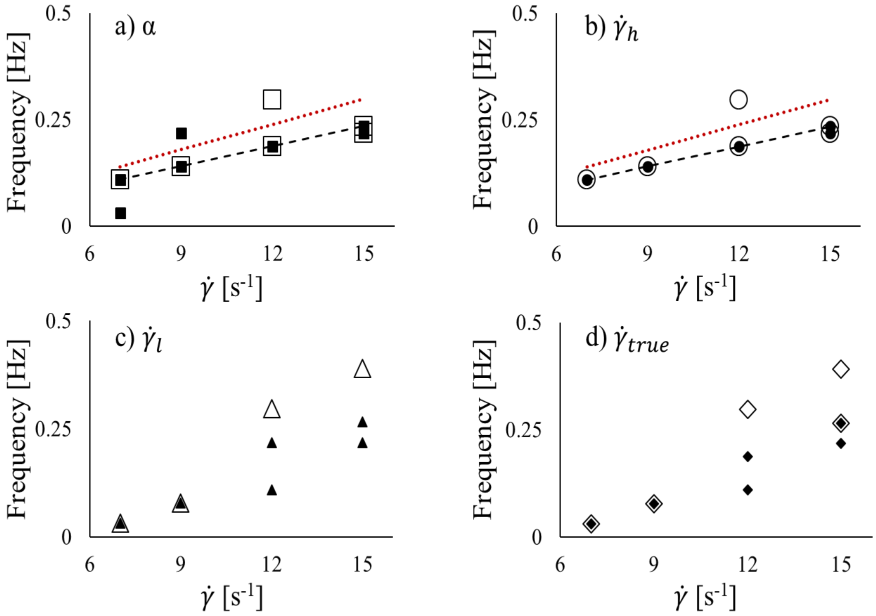

Figure 10: The dominant frequencies in the spectra for protocol 1 (filled symbols) and protocol 2 (open symbols) plotted as a function of applied shear rate for (a) the interface position α (b) the shear rate in the high shear band $\dot{\gamma}_h$, (c) the shear rate in the low shear band $\dot{\gamma}_l$ and (d) the true shear rate $\dot{\gamma}_{true}$. Red dashed lines show rotation frequencies corresponding to the applied shear rates, while black dashed lines correspond to the linearly varying rotationally correlated observed frequencies.

cols and varies linearly with the applied shear rate (indicated by the dashed black line). This frequency scales with the velocity of the inner rotating cylinder, it is equal to $v_{max}/64$. Due to small mechanical imperfections, the rotation can be slightly asymmetrical. In this Couette cell, these imperfections are very small, well below the spatial resolution of the images, and do not impact measurements in Newtonian fluids. Shear start-up experiments under these exact conditions were conducted with water and fluctuation frequencies were not observed. However, since the WLM samples are viscoelastic and hydrodynamically unstable, a frequency dependent upon the rotation arises in the data. Note the observed frequency is not equal to the frequency of rotation ($f = v_{max}/2\pi R_i$), shown by the red dashed lines in Figures 10(a) and (b), but is correlated with the rotation rate, and deviates more as the applied shear rate increases. Henceforth this will be referred to as the rotationally correlated frequency. Such a rotationally correlated frequency has also been observed previously. Lerouge *et al.* observed time periodic oscillations in interface position following shear start up for 11% CTAB and attributed one frequency of oscillation to rotation [41].

While the fluctuations are influenced by the rotation rate because the flow is highly elastic and unstable, other frequencies are also amplified and appear at specific shear rates. The fluctuation frequencies will be influenced by effects due to the presence of three-dimensional flow, *i.e.* the vortices in the high shear band, interacting with the frequency of rotation. It is the interplay between the rotation, the vortex size and the movement (traveling) of the vortices that causes fluctuations in the 1D measurement with time. Note that for both protocols, the low shear rate and the true shear rate have nearly all the same frequencies (Figures 10c and d). For CTAB solutions, Decruppe *et al.* have shown that low shear rate and the amount of slip is correlated for time averaged velocity profiles as a function of applied shear rate [42]. It is not surprising therefore that the fluctuations in these characteristics with time at a constant applied shear rate would be coupled as well.

In Figures 11(a) and (b), dominant frequencies for all shear banding characteristics are plotted against each other for protocol 1 and 2 respectively. We can see that preshear, as would be expected, does not impact the rotationally correlated frequency seen in interface position α and high shear rate $\dot{\gamma}_h$ (dashed lines). However, the trends in other frequencies with increasing applied shear rate for $\dot{\gamma}_l$ and $\dot{\gamma}_{true}$ differ with pre-shear. For both protocols, we see a transition from frequencies lower than the rotationally correlated frequency to higher as applied shear rate increases. When pre-shear is present (protocol 2), this transition occurs at a lower applied shear rate. It is clear that pre-shear and the corresponding disruption to the equilib-

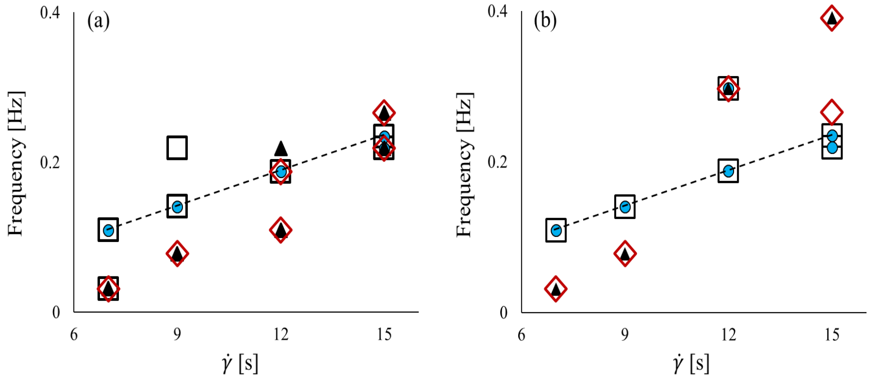

Figure 11: Dominant frequencies for α (open black squares), $\dot{\gamma}_h$ (closed blue circles), $\dot{\gamma}_l$ (closed black triangles) and $\dot{\gamma}_{true}$ (open red diamonds) for (a) protocol 1 (no pre-shear) and (b) protocol 2 (with pre-shear). Dashed lines correspond to the rotationally correlated frequencies.

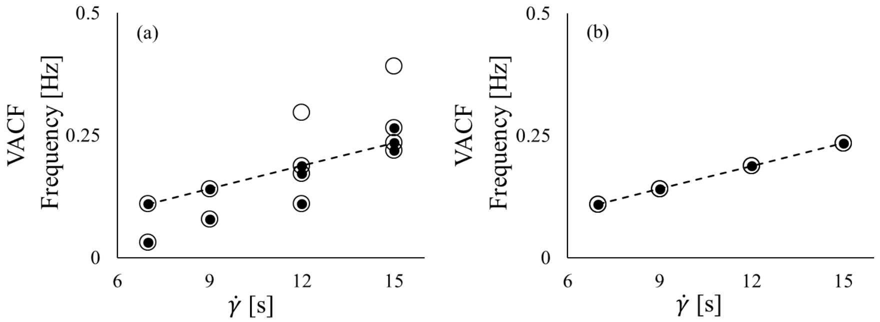

Figure 12: The dominant frequencies in the velocity autocorrelation function (VACF) spectra plotted as a function of applied shear rate for (a) the velocity in the spatial center of the high shear band and (b) the velocity in the spatial center of the low shear band. Filled black circles are protocol 1 and open circles are protocol 2. Dashed lines correspond to the rotationally correlated frequencies.

rium wormlike micelle microstructure impacts the fluctuation, more specifically the fluctuation in the low shear and true shear rates and their trend with applied shear rate. As we have discussed, with pre-shear the high shear band is smaller, *i.e.* the interface position is located closer to the inner rotating wall, and therefore vortex sizes are smaller, possibly impacting the interplay between vortex size and traveling rate and altering the resultant frequencies. The differences in frequency trends with applied shear rate between the protocols may be further evidence of more complicated instability due to the presence of pre-shear. Further investigation is required to elucidate such connections.

We can also do this Fourier Transform analysis directly on the time velocity autocorrelation functions [17], rather than the characteristics obtained through fitting of the velocity profile. Figure 12 shows the extracted dominant frequencies obtained with this analysis as a function of applied shear rate, comparing protocol 1 (the closed circles) and protocol 2 (open circles), for a velocity located in middle of the high shear band (Figure 12a) and in the middle of the low shear band (Figure 12b).

The low shear band velocity, which is stable and does not have vortices, has only the rotationally correlated frequencies. This shows that the impact of the periodicity of the inner rotating cylinder is propagated through the entire viscoelastic fluid, a memory effect not present in Newtonian fluids. The velocity in the high shear band, which is experiencing the actual three-dimensional flow (both 3D vorticial structure and vortex traveling) shows multiple frequencies, including the rotationally correlated frequency.

Considering Figure 12(a), we are observing fluctuations in velocity at a particular position within the fluid gap, rather than fluctuations of a fitted parameter covering the entire high shear band and coupled with other shear banded characteristics. Therefore, the fluctuation frequencies directly depend on the secondary flow due to the vortices and the traveling of the vortices within the 10 mm slice, as well as the bulk rotation. The velocity in the more stable low shear band, where no vortices are present, is not impacted directly by the vortices, unlike the low shear rate fitted parameter. Again, the differences between protocol 1 and protocol 2 are evident at the higher applied shear rates.

4 Conclusions

1D velocity profiles acquired every 1 s across the fluid gap of a Rheo-NMR Couette geometry under shear startup conditions for protocols without pre-shear and with pre-shear were analyzed to quantify the characteristics of the shear banded flow and the evolution from transient to steady state shear banding. Timescales to reach steady state were extracted for all shear banding characteristics (α, $\dot{\gamma}_h$, $\dot{\gamma}_l$, and $\dot{\gamma}_{true}$). There was little difference in timescale between the protocols, indicating that pre-shear does not impact the time it takes for the flow to reach a steady state. Timescales to reach steady state were found to decrease as the applied shear rate increased.

General shear banding behavior was impacted by the presence of pre-shear. When pre-shear was applied, the interface position was consistently located nearer the inner rotor wall than without pre-shear. There was also a more gradual increase in interface position with increasing applied shear rate, as well as a corresponding decrease in the low shear rate, than was observed without pre-shear. Without pre-shear, a more standard lever rule behavior was observed with linearly increasing interface position and a largely constant shear rate in the low shear band. For both the high shear rate and the true shear rate, there was very little difference between the two protocols, with both characteristics increasing with increasing applied shear rate. Pre-shear, which disrupts and homogenizes equilibrium structure, influences primarily the values of low shear rate and location of the interface.

The 1D velocity profiles and therefore shear banding characteristics exhibit large temporal fluctuations. It is well documented in the literature that in the high shear band pairs of Taylor vortices stacked in the vorticial direction manifest in this system due to elastic instabilities [39]. The temporal fluctuations in the 1D measurement are at least in part a reflection of the coherent 3D nature of the flow. Frequencies of fluctuation were extracted for the four characteristics of shear banding as well as for specific velocities within the high and low shear band by Fourier Transform of the time and velocity autocorrelation functions.

The fluctuations with time in the shear banding characteristics are coupled, *i.e.* secondary flow due to Taylor vortices would impact the fluctuating value of shear rate in the high shear band obtained through fitting of the velocity profile, but also causes undulations in interface position along the vorticity direction that manifests as fluctuation frequencies. We analyzed correlations between fluctuation frequency and applied shear rate and concluded that fluctuation frequencies depended on an interplay between effects due to rotation of the inner cylinder and effects which are due to spatially averaged aspects of a time dependent three-dimensional flow (*i.e.* vortex size and traveling of the vortices) as has been observed in the literature. Depending on where in the stress plateau the applied shear rate falls, different effects dominate, changing the value and number of frequencies, as well as the correlation with applied shear rate. For the velocity fluctuations, the stable low shear band showed only a single frequency, while the high shear band, where the coherent 3D flow occurs, multiple frequencies were observed.

Further research is needed to investigate these trends in fluctuation frequency in order to further quantify the underlying mechanisms. Next steps would be to extend this analysis to additional concentrations, different types of WLM systems and other flow protocols with the goal of identifying correlations between fluctuation frequency and features of the shear banding and elastic instability. This analysis could provide a way to detect and quantify 3D flow patterns from a 1D measurement.

Acknowledgement: JRB acknowledges the NSF (1543875) for funding. RA acknowledges the Higher Committee for Education Development in Iraq (HREC) for fellowship funding. JRB, SLC and JDS acknowledge the M. J. Murdoch charitable trust for equipment funding.

Author contribution statement: In this study, Rehab Al-kaby has carried out experiments under the help of other authors. All the authors contributed to the analysis and the interpretation of the data. All authors have involved in preparation and providing of the final manuscript.

References

[1] Larson RG. The Structure and Rheology of Complex Fluids. New York: Oxford University Press; 1999.

[2] Rehage H, Hoffmann H. Rheological properties of viscoelastic surfactant systems. J Phys Chem. 1988;92(16):4712–9.

[3] Cates ME, Evans MR. Soft and fragile matter: nonequilibrium dynamics, metastability and flow (PBK). CRC Press; 2000. https://doi.org/10.1887/0750307242.

[4] Cromer M, Fredrickson GH, Leal LG. A study of shear banding in polymer solutions. Phys Fluids. 2014;26(6):063101.

[5] Gilbreth C, Sullivan S, Dennin M. Flow transitions in two-dimensional foams. Phys Rev E Stat Nonlin Soft Matter Phys. 2006 Nov;74(5 Pt 1):051406.

[6] Lerouge S, Berret JF. Shear-Induced Transitions and Instabilities in Surfactant Wormlike Micelles. In: Dusek K, Joanny JF, editors. Polymer Characterization: Rheology, Laser Interferometry, Electrooptics. Berlin: Springer-Verlag Berlin; 2010. pp. 1–71.

[7] Angelico R, Olsson U, Palazzo G, Ceglie A. Surfactant curvilinear diffusion in giant wormlike micelles. Phys Rev Lett. 1998;81(13):2823–6.

[8] Ezrahi S, Tuval E, Aserin A. Properties, main applications and perspectives of worm micelles. Adv Colloid Interface Sci. 2006 Dec;128-130:77–102.

[9] Maitland GC. Oil and gas production. Curr Opin Colloid Interface Sci. 2000;5(5-6):301–11.

[10] Yang J. Viscoelastic wormlike micelles and their applications. Curr Opin Colloid Interface Sci. 2002;7(5-6):276–81.

[11] Dreiss CA. Wormlike micelles: where do we stand? Recent developments, linear rheology and scattering techniques. Soft Matter. 2007;3(8):956–70.

[12] Cates M. Nonlinear viscoelasticity of wormlike micelles (and other reversibly breakable polymers). J Phys Chem. 1990;94(1):371–5.

[13] Rehage H, Hoffmann H. Viscoelastic surfactant solutions: model systems for rheological research. Mol Phys. 1991;74(5):933–73.

[14] Hu YT, Lips A. Kinetics and mechanism of shear banding in an entangled micellar solution. J Rheol (NYNY). 2005;49(5):1001–27.

[15] Lerouge S, Decruppe JP, Olmsted P. Birefringence banding in a micellar solution or the complexity of heterogeneous flows. Langmuir. 2004 Dec;20(26):11355–65.

[16] Radulescu O, Olmsted PD, Decruppe JP, Lerouge S, Berret JF, Porte G. Time scales in shear banding of wormlike micelles. Europhys Lett. 2003;62(2):230–6.

[17] López-González MR, Holmes WM, Callaghan PT, Photinos PJ. Shear banding fluctuations and nematic order in wormlike micelles. Phys Rev Lett. 2004 Dec;93(26 Pt 1):268302.

[18] Lettinga MP, Manneville S. Competition between shear banding and wall slip in wormlike micelles. Phys Rev Lett. 2009 Dec;103(24):248302.

[19] Lopez-Gonzalez MR, Holmes WM, Callaghan PT. Rheo-NMR phenomena of wormlike micelles. Soft Matter. 2006;2(10):855–69.

[20] Fardin MA, Lerouge S. Instabilities in wormlike micelle systems. From shear-banding to elastic turbulence. Eur Phys J E Soft Matter. 2012 Sep;35(9):91.

[21] Manneville S, Bécu L, Colin A. High-frequency ultrasonic speckle velocimetry in sheared complex fluids. Eur Phys J Appl Phys. 2004;28(3):361–73.

[22] Bécu L, Anache D, Manneville S, Colin A. Evidence for three-dimensional unstable flows in shear-banding wormlike micelles. Phys Rev E Stat Nonlin Soft Matter Phys. 2007 Jul;76(1 Pt 1):011503.

[23] Fischer E, Callaghan PT. Is a birefringence band a shear band? Europhys Lett. 2000;50(6):803–9.

[24] Salmon JB, Colin A, Manneville S, Molino F. Velocity profiles in shear-banding wormlike micelles. Phys Rev Lett. 2003 Jun;90(22):228303.

[25] Fardin MA, Divoux T, Guedeau-Boudeville MA, Buchet-Maulien I, Browaeys J, McKinley GH, et al. Shear-banding in surfactant wormlike micelles: elastic instabilities and wall slip. Soft Matter. 2012;8(8):2535–53.

[26] Fardin MA, Casanellas L, Saint-Michel B, Manneville S, Lerouge S. Shear-banding in wormlike micelles: beware of elastic instabilities. J Rheol (NYNY). 2016;60(5):917–26.

[27] Fardin MA, Ober TJ, Grenard V, Divoux T, Manneville S, McKinley GH, et al. Interplay between elastic instabilities and shear-banding: three categories of Taylor-Couette flows and beyond. Soft Matter. 2012;8(39):10072–89.

[28] Perge C, Fardin MA, Manneville S. Surfactant micelles: model systems for flow instabilities of complex fluids. Eur Phys J E Soft Matter. 2014 Apr;37(4):23.

[29] Taylor GI. Stability of a Viscous Liquid Contained between Two Rotating Cylinders. Philosophical Transactions of the Royal Society of London. Series A, Containing Papers of a Mathematical or Physical Character (1896-1934), 1923. **223**(605): p. 289-343.

[30] Al-kaby RN, Jayaratne JS, Brox TI, Codd SL, Seymour JD, Brown JR. Rheo-NMR of transient and steady state shear banding under shear startup. J Rheol (NYNY). 2018;62(5):1125–34.

[31] Berret JF, Roux DC, Porte G. Isotropic-to-nematic transition in wormlike micelles under shear. J Phys II. 1994;4(8):1261–79.

[32] Callaghan PT. Translational Dynamics and Magnetic Resonance: Principles of Pulsed Gradient Spin Echo NMR. New York: Oxford University Press; 2011. https://doi.org/10.1093/acprof:oso/9780199556984.001.0001.

[33] Rogers S, Callaghan P. Time-dependent NMR-velocimetry of a colloidal glass. Rheol Acta. 2009;48(7):735–45.

[34] López-Barrón CR, Gurnon AK, Eberle AP, Porcar L, Wagner NJ. Microstructural evolution of a model, shear-banding micellar solution during shear startup and cessation. Phys Rev E Stat Nonlin Soft Matter Phys. 2014 Apr;89(4):042301.

[35] Macosko CW. Rheology : principles, measurements, and applications. New York (New York): Wiley-VCH; 1994.

[36] Fardin MA, Lerouge S. Instabilities in wormlike micelle systems. From shear-banding to elastic turbulence. Eur Phys J E Soft Matter. 2012 Sep;35(9):91.

[37] Glasgow LA. Transport phenomena: an introduction to advanced topics. John Wiley & Sons; 2010. https://doi.org/10.1002/9780470626610.

[38] Berret JF, Roux DC, Lindner P. Structure and rheology of concentrated wormlike micelles at the shear-induced isotropic-to-nematic transition. Eur Phys J B. 1998;5(1):67–77.

[39] Fardin MA, Lasne B, Cardoso O, Grégoire G, Argentina M, Decruppe JP, et al. Taylor-like vortices in shear-banding flow of giant micelles. Phys Rev Lett. 2009 Jul;103(2):028302.

[40] Kose K. Spatial mapping of velocity power spectra in Taylor-Couette flow using ultrafast NMR imaging. Phys Rev Lett. 1994 Mar;72(10):1467–70.

[41] Lerouge S, Argentina M, Decruppe JP. Interface instability in shear-banding flow. Phys Rev Lett. 2006 Mar;96(8):088301.

[42] Decruppe JP, Greffier O, Manneville S, Lerouge S. Local velocity measurements in heterogeneous and time-dependent flows of a micellar solution. Phys Rev E Stat Nonlin Soft Matter Phys. 2006 Jun;73(6 Pt 1):061509.